Struct Multidisc Optim (2009) 38:301–316
DOI 10.1007/s00158-008-0292-x

INDUSTRIAL APPLICATION

Aeroelastic topology optimization of membrane structures for micro air vehicles

Bret Stanford · Peter Ifju

Received: 7 March 2008 / Revised: 2 May 2008 / Accepted: 10 June 2008 / Published online: 19 July 2008

Abstract This work considers the aeroelastic optimization of a membrane micro air vehicle wing through topology optimization. The low aspect ratio wing is discretized into panels: a two material formulation on the wetted surface is used, where each panel can be membrane (wing skin) or carbon fiber (laminate reinforcement). An analytical sensitivity analysis of the aeroelastic system is used for the gradient-based optimization of aerodynamic objective functions. An explicit penalty is added, as needed, to force the structure to a 0–1 distribution. The dependence of the solution upon initial design, angle of attack, mesh density, and objective function are presented. Deformation and pressure distributions along the wing are studied for various load-augmenting and load-alleviating designs (both baseline and optimized), in order to establish a link between stiffness distribution and aerodynamic performance of membrane micro air vehicle wings. The work concludes with an experimental validation of the superiority of select optimal designs.

Keywords Micro air vehicle · Topology optimization · Aeroelastic membrane wing

Nomenclature

$\mathbf{a}$	adjoint vector
$\mathbf{A}$	aeroelastic Jacobian
α	angle of attack
b	wingspan
β	small number to prevent singularity
c	root chord
$\mathbf{C}$	vortex lattice influence matrix
C_D	drag coefficient
C_L	lift coefficient
$C_{\mathrm{L}\alpha}$	lift slope
$C_{\mathrm{m}\alpha}$	pitching moment slope
D	carbon fiber flexural rigidity
g	objective function
$\mathbf{G}$	aeroelastic system of equations
$\mathbf{\Gamma}$	horseshoe vortex circulations
$\mathbf{K}$	reduced global stiffness matrix
$\mathbf{K}_\mathrm{e}$	element stiffness matrix
$\mathbf{K}_\mathrm{p}$, $\mathbf{K}_\mathrm{m}$	carbon fiber and membrane stiffness matrices
$\mathbf{L}$	vortex lattice source vector
L/D	efficiency
$\mathbf{n}$	wing outward normal
p	nonlinear power law
$\mathbf{P}$, $\mathbf{Q}$	interpolation matrices
$\mathbf{r}$	aeroelastic response
R	penalty parameter
$\mathbf{S}$	sensitivity of objective function to vortex circulations
T	in-plane membrane pre-stress resultant
$\mathbf{u}$	solution to finite element analysis
u_o, v_o, w_o	induced velocities
U_∞	free-stream velocity
w	out-of-plane displacement
x, y	chordwise and spanwise position
$\mathbf{X}$	element densities
$\mathbf{z}_\mathrm{o}$, $\mathbf{z}$	rigid and flexible wing shapes

B. Stanford (✉) · P. Ifju
Department of Mechanical and Aerospace Engineering,
University of Florida, Gainesville, FL 32611, USA
e-mail: bstan@ufl.edu

1 Introduction

This work considers the design of flexible micro air vehicle wings (MAVs, with a wingspan less than 15 cm) through aeroelastic topology optimization. The structure for these vehicles resemble larger hang gliders and sail wings (Ormiston 1971): a flexible membrane surface (latex rubber, in this case) strategically reinforced with stiffer rib and batten structures (carbon fiber laminates). The flight performance of flexible MAVs has indicated several desirable properties directly attributable to the elastic nature of the wing: primarily, passive shape adaptation (Albertani et al. 2007). Depending upon the nature of the laminate reinforcement (of which the trailing edge is particularly important), the wing deformation may be able to alleviate the flight loads (which may reduce the drag, delay stall, or provide gust rejection) or augment the flight loads (higher lift, longer static stability margins). Either methodology may be preferred (or perhaps a compromise between the two), depending upon flight environment (indoor or outdoor flight), payload, propulsion, range and duration requirements. This problem can be solved by discretizing the wing into panels for an aeroelastic topology optimization study, with a two-material formulation (each panel can be stiff carbon fiber laminate or flexible latex membrane) on the wetted surface of the wing. A series of aerodynamic objective functions can be considered, including L/D, C_{L}, C_{D}, $C_{\mathrm{L}\alpha}$, and $C_{\mathrm{m}\alpha}$.

The basics of topology optimization are given by Zuo et al. (2007): the design domain is discretized, and the relative density of each element can be 0 (void) or 1 (solid). Early work in this field optimizes a structure under static loads by minimizing the compliance with an equality constraint upon the volume fraction, though applications of topology optimization have expanded dramatically in recent years. A review of the extensive and disparate applications that have been successfully solved with topology optimization is given by Eschenauer and Olhoff (2001), Bendsøe and Sigmund (2003), and Bendsøe et al. (2005).

Solving a topology optimization scheme with strictly discrete design variables is rare; Anagnostou et al. (1992) utilize simulated annealing, while Deb and Goel (2001) and Wang et al. (2006) use a genetic algorithm (with the latter paper providing a detailed literature review of the topic). Beckers (1999) uses a dual method to solve the large-scale discrete problem, while recent work by Stolpe and Stidsen (2006) use a hierarchical technique: the topology optimization problem is solved on successively refined meshes. The optimum obtained from the previous coarse mesh is used as a good starting point for a local search algorithm, solved as a convex mixed 0–1 program. The computational requirements of such binary techniques can be severe for even moderately-sized problems, however. A more-commonly utilized strategy lets the density vary continuously between 0 and 1 and then penalizes intermediate values during the optimization (Bendsøe and Sigmund 2003), and is used for this work.

As noted by Stegmann and Lund (2005a), solid-void topology optimization of engineering shell structures has little practical relevance: holes in the structure can depreciate the ability of the structure to carry membrane loads, and may be completely forbidden out of aerodynamic considerations. Two (or more) material formulations can potentially be used; interpolation schemes for such a model are given by Bendsøe and Sigmund (2003), and a similar interpolation is used in this work. Alternatively, layered shell models may be used, by constructing the shell from a combination of solid layers and artificial layers (which may or may not be void). As discussed by Lee et al. (2000), the layup can use single artificial layers (potentially resulting in holes), two layers for an eccentric stiffness about the mid-surface, or three layers with potential enclosed voids or holes concentric to the midplane. This work is extended by Stegmann and Lund (2005b), who locate the optimal distribution of glass/epoxy laminate and polymeric foam in a shell structure, as well as the fiber angles of the former.

From a literature standpoint, aeronautical applications of topology optimization of structures are rare; aeroelastic applications are rarer still. The literature can be roughly divided into three categories. The first uses an aerodynamic solver to compute the pressure distribution over the wing (during steady flight, pull-up maneuvers, etc). This load distribution is then applied to the structure for optimization: global metrics such as compliance, weight/volume fraction, and vibration frequency or local metrics such as displacement and stress objective functions and constraints can all be considered. The re-distribution of the aerodynamic loading due to elastic wing deformation is ignored. The second category explicitly uses the aerodynamic performance of a flexible wing for objective functions or constraints, and necessarily includes aeroelastic coupling. The third category is topology optimization of channel flows: changes in the force imparted by a fluid flow are not made with flexible structures, but by dividing the computational domain into either fluid or solid elements.

Literature indicative of the first category can be found in the work of Balabanov and Haftka (1996), who optimize the internal structure of a transport wing, using a ground structure approach (the domain is filled

with interconnected trusses, and the cross-sectional area of each is a design variable (Bendsøe and Sigmund 2003)) for compliance minimization. Eschenauer and Olhoff (2001) optimize the topology of an internal wing rib under both pull-up load maneuvers and internal tank pressures, using a bubble method. Krog et al. (2004) also optimize the topology of wing box ribs, and discuss methods for interpretation of the results to form an engineering design, followed by sizing and shape optimization. Luo et al. (2006) compute the optimal topology of an aerodynamic missile body, considering both static loads and natural frequencies.

Aeroelastic topology optimization (second category discussed above) is an under-served method of aircraft design, presumably due to the large computational cost associated with such an undertaking. The seminal work in this field is given by Maute and Allen (2004), who consider the topological layout of stiffeners within a swept wing, using a three-dimensional Euler solver coupled to a linear finite element model. Results from an adjoint sensitivity analysis of the coupled aeroelastic system (Maute et al. 2002; Martins et al. 2001) are fed into an augmented Lagrangian optimizer to minimize mass with constraints upon the lift, drag, and wing displacement. The authors are able to demonstrate the superiority of designs computed with aeroelastic topology optimization, rather than considering a constant pressure distribution. This research effort is extended by Maute and Reich (2006) for topology optimization of a compliant morphing mechanism within an airfoil, considering both passive and active shape deformations. Superior optima are found with this method, as compared to a jig-shape approach: optimizing the aerodynamic shape, and then locating the mechanism that leads to such a shape. Very recent work is given by Gomes and Suleman (2008), who use a spectral level set method to maximize aileron reversal speed by reinforcing the upper skin of a wing torsion box via topology optimization.

For the third category listed above, early work in the topology optimization of fluid flows is given by Borrvall and Petersson (2003), who divide the design domain into fluid and solid elements. Flow is assumed to be governed by Stoke's differential equations for creeping planar flows. Interpolation between fluid and solid is obtained by means of the distance between the two surfaces that contain the fluid. Gersborg-Hansen et al. (2005) extend this technique to account for fluid inertia in the governing equations, thus utilizing a nonlinear flow model. Pingen et al. (2007) find the minimum drag profile of submerged bodies, using a lattice Boltzmann method as an approximation to the Navier–Stokes equations. Drag is minimized by a football shape (with front and back angles of 90°) at low Reynolds numbers (where reducing surface area is important), and a symmetric airfoil at higher Reynolds numbers (where streamlining is more important).

The research detailed in this work is solely concerned with the second category discussed above: aeroelastic topology optimization of a thin flexible micro air vehicle wing. This work details the location of holes within a carbon fiber wing shell, holes which will then be covered with a thin, taught, rubber membrane skin. Numerically, the wing will be discretized into a series of panels, wherein each panel can be a carbon fiber laminated shell or an extensible latex rubber skin. The wing's performance is determined by a static aeroelastic solver, and objective functions consist of lift, drag, and pitching moment-based aerodynamic metrics. Nonlinear interpolation schemes allow each wing panel to vary continuously between carbon fiber skeleton and rubber membrane skin, necessitating an adjoint sensitivity analysis of the coupled aeroelastic system.

The remainder of this work is organized as follows. A brief description of membrane micro air vehicle aeroelasticity is given, followed by details of the topology optimization within the wing structure, and how the technique fits into the overall design scheme required for MAVs. This is followed by the computational framework: material interpolation, the static aeroelastic model, sensitivity analysis, and optimization procedures. Results are then given in terms of convergence histories, and the dependence of the optimal design (upon initial design, flight conditions, mesh density, and objective functions). Lift generation as seen by the topology optimizer is examined in detail, in order to elucidate several load-alleviating and -augmenting mechanisms. The work is concluded with an experimental validation of the superiority of select optimal designs over baseline wing structures.

2 Membrane micro air vehicle wings

Two extensively-flight tested membrane wing topologies are given in Fig. 1. On the left of the figure is a batten-reinforced wing design (BR), where three carbon fiber strips (battens) are imbedded into each membrane semi-wing. The trailing edge of this design is permitted to lift up due to an applied pressure load. The nose-down geometric twist of each wing section will alleviate the flight loads, and possibly decrease C_{D}, and $C_{\mathrm{L}\alpha}$ (as compared to a rigid wing; Albertani et al. 2007). Conversely, on the right side of Fig. 1 is a perimeter-reinforced wing design (PR). Now the

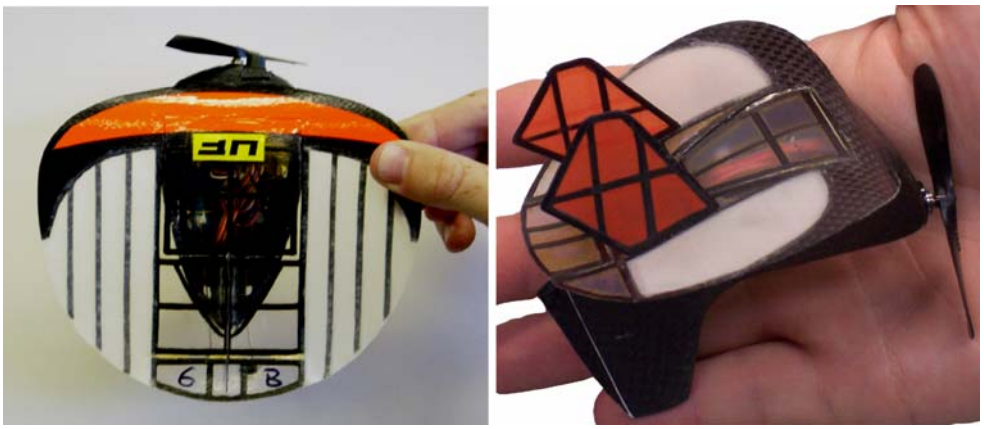

Fig. 1 Batten-reinforced (*left*) and perimeter-reinforced (*right*) membrane wing designs

trailing edge is constrained by a laminate perimeter, and the membrane skin will inflate due to an applied load. This aerodynamic twist of each flexible wing section will augment the flight loads, and possibly increase C_L and decrease $C_{m\alpha}$ (Albertani et al. 2007).

A rigorous aeroelastic topology optimization of the membrane wings may be able to produce structures that out-perform these two designs. A fairly fine structural grid is needed to resolve topologies on the order of those seen in Fig. 1, which will, of course, increase the computational cost associated with the optimization. The wing is discretized into a set of quadrilaterals, which represent the density variables: 0 or 1. These quadrilaterals are used as panels for the aerodynamic solver, and broken into two triangles for the finite element solver, as shown in Fig. 2. As in Fig. 1, the wing topology at the root, leading edge, and wing tip is fixed as carbon fiber, to maintain some semblance of an aerodynamic shape capable of sustaining lift. The wing topology in the figure is randomly distributed.

It should also be noted that aeroelastic topology optimization is one of many techniques that should be taken into account when designing a micro air vehicle: Torres (2002), for example, minimizes a combination of payload, endurance, and agility metrics, with wing/tail planform, aspect ratio, propeller location, and angle of attack variables. This work fixes all of these variables, and only considers un-constrained single-objective topology optimization of longitudinal aerodynamic performance metrics. The goal of this research is to provide insight into the complex relationship between stiffness distribution and aerodynamic behavior of a membrane MAV wing, with the future goal of utilizing this technique as part of a larger, global design scheme.

3 Computational framework

3.1 Material interpolation

Topology optimization with continuous density variables may require a mechanism to push the final structure to a 0–1 distribution. An implicit penalty upon intermediate densities can be achieved through a nonlinear power law interpolation. This technique is known as the solid isotropic material with penalization method, or SIMP (Zuo et al. 2007). The power law's effectiveness as an implicit penalty is predicated upon a volume constraint: intermediate densities are unfavorable, as their stiffness is small compared to their volume (Bendsøe and Sigmund 2003). For the two-material wing considered above (membrane or carbon

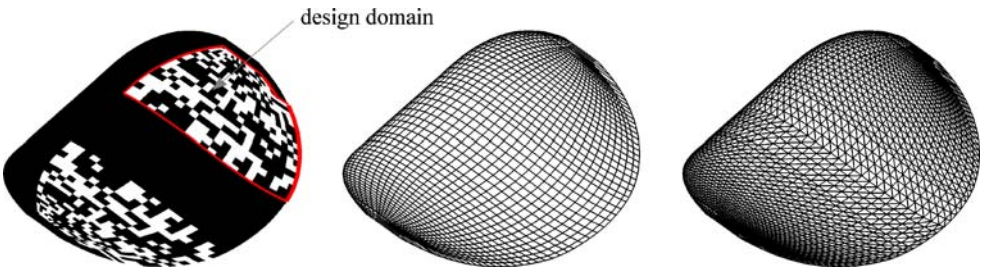

Fig. 2 Sample wing topology (*left*), aerodynamic mesh (*center*), and structural mesh (*right*)

fiber), the stiffness matrix $\mathbf{K}_e$ of each finite element in Fig. 2 can be computed as:

$$\mathbf{K}_e = \left(\mathbf{K}_p \cdot (1-\beta) - \mathbf{K}_m\right) \cdot X_e^p + \mathbf{K}_m + \beta \cdot \mathbf{K}_p \quad (1)$$

where $\mathbf{K}_p$ and $\mathbf{K}_m$ are the plate and membrane elements, respectively (the latter with zeros placed within rows and columns corresponding to bending degrees of freedom). β is a small number used to prevent singularity in the pure membrane element (due to the bending degrees of freedom), $\mathbf{X}_e$ is the density of the element, varying from 0 (membrane) to 1 (carbon fiber), and p is the nonlinear penalization power.

No volume constraint is utilized here, due to an uncertainty upon what this value should be. Furthermore, for aeronautical applications it may be desired to minimize the mass of the wing itself, as discussed by Maute and Allen (2004). Regardless, the nonlinear power law of SIMP is still useful for the current application, as demonstrated in Fig. 3. Both linear and nonlinear material interpolations are given for the lift computation (the aeroelastic model used here is described below), and the wing topology is altered uniformly.

For the linear interpolation (i.e., without SIMP), the aeroelastic response is a weak function of the density until $\mathbf{X}$ becomes very small (~0.001), when the system experiences a very sharp change as $\mathbf{X}$ is further decreased to 0. This is a result of the large stiffness imbalance between the carbon fiber laminates and the membrane skin, and the fact that lift is a direct function of the wing's compliance (the inverse of the weighted sum of the two disparate stiffness matrices). The inclusion of a nonlinear penalization power ($p = 5$), spreads the response evenly between 0 and 1: at $\mathbf{X} = 0$ and 1, both linear and nonlinear interpolation curves coincide. Aeroelastic topology optimization with linear material interpolation experiences convergence difficulties, as the gradient-based technique struggles with the nearly-disjointed design space; a penalization power of 5 is utilized for the remainder of this work. It can also be seen in Fig. 3 that the sensitivity of the aeroelastic response to element density is zero for a pure membrane wing ($\mathbf{X} = 0$), as can be inferred from the interpolation equation above. As such, using a pure membrane wing as an initial guess for optimization will not work, as the design won't change.

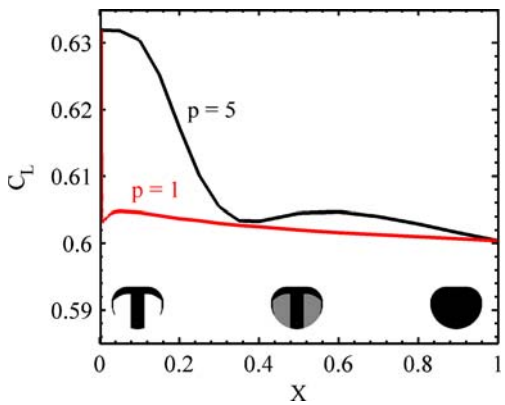

Fig. 3 Effect of linear and nonlinear material interpolation upon lift

Two local optima exist in the design space of Fig. 3, which may prevent the gradient-based optimizer from converging to a 0–1 material distribution. To counteract this problem, an explicit penalty on intermediate densities is added to the objective function (Chen and Wu 2008):

$$R \cdot \sum_{i=1}^{N_X} \sin\left(X_i \cdot \pi\right) \quad (2)$$

where R is a penalty parameter appropriately sized so as not to overwhelm the aerodynamic performance of the wing topology. Several potential issues may appear with this formulation: the inclusion of a large penalty early in the optimization process will upset the compromise between improving the aerodynamic performance and removing intermediate densities. In order to prevent such interference, this penalty is only added when and if the aeroelastic optimizer has converged upon a design with intermediate densities. R is sized such that the penalty is 10–15% of the objective function, and is not increased during the optimization process. Such a strategy is not found to significantly alter the optimal topology, as will be discussed below.

3.2 Static aeroelastic analysis

Due to the large number of expected function evaluations (~200) needed to converge upon an optimal wing topology, and the required aeroelastic sensitivities (computed with an adjoint method), a lower-fidelity aeroelastic model is used for the current application. The membrane elements within the wing structure are assumed to obey Poisson's differential equation for a taught elastic membrane subjected to a transverse distributed pressure (Cook et al. 2002):

$$\nabla^2 w = -p/T \quad (3)$$

where p is the applied pressure, w is the out-of-plane displacement, and T is the in-plane pre-stress resultant. This linear membrane model is known to be accurate, as long as the plane strains that develop within the elastic sheet due to the pressure loading are much smaller than the original pre-strains. Discretization of the wing

into finite elements leaves one degree of freedom per membrane node: the out-of-plane displacement w. Similarly, the carbon fiber elements within the wing are assumed to be governed by:

$$\nabla^4 w = p/D \tag{4}$$

where D is the plate's flexural rigidity, and the orthotropy of the plain weave laminate is ignored. Each node of a plate element will have three degrees of freedom: one out-of-plane displacement, and two rotations. The finite element mesh is seen on the right of Fig. 2.

A linear vortex lattice method is used to compute the aerodynamic pressure distribution over the flexible wing. The continuous distribution of bound vorticity is approximated by discretizing the wing into a paneled grid, and placing a horseshoe vortex upon each panel. Each horseshoe vortex is comprised of a bound vortex (which coincides with the quarter-chord line of each panel), and two trailing vortices extending downstream. Each vortex filament creates a velocity whose magnitude is assumed to be governed by the Biot–Savart law (Katz and Plotkin 2001). Furthermore, a control point is placed at the three-quarter-chord point of each panel. The tangency condition is applied (i.e., the wing becomes a streamline of the flow) by stipulating that the induced flow (from the horseshoe vortices) along the outward normal at each control point exactly cancels with that caused by the free-stream velocity. The following system of equations results:

$$\begin{bmatrix} \mathbf{C}_{11} & \mathbf{C}_{12} & \cdots & \mathbf{C}_{1N} \\ \mathbf{C}_{21} & \mathbf{C}_{22} & \cdots & \mathbf{C}_{2N} \\ \vdots & \vdots & \ddots & \vdots \\ \mathbf{C}_{N1} & \mathbf{C}_{N2} & \cdots & \mathbf{C}_{NN} \end{bmatrix} \cdot \begin{Bmatrix} \mathbf{\Gamma}_1 \\ \mathbf{\Gamma}_2 \\ \vdots \\ \mathbf{\Gamma}_N \end{Bmatrix} = - \begin{Bmatrix} \{U_\infty \cos(\alpha), 0, U_\infty \sin(\alpha)\} \cdot n_1 \\ \{U_\infty \cos(\alpha), 0, U_\infty \sin(\alpha)\} \cdot n_2 \\ \vdots \\ \{U_\infty \cos(\alpha), 0, U_\infty \sin(\alpha)\} \cdot n_N \end{Bmatrix} \tag{5}$$

The source vector in (5) assumes longitudinal flow (no side-slip): U_∞ is the free-stream velocity, α the angle of attack of the wing, and n_i the outward normal of the wing at the ith control point. Γ_i is the unknown circulation strength of each horseshoe vortex, and the influence coefficients are given by:

$$C_{ij} = \{u_o, v_o, w_o\}_{ij} \cdot n_i \tag{6}$$

where $u_{o,ij}$, $v_{o,ij}$, and $w_{o,ij}$ are the velocities induced at the ith control point by the jth horseshoe vortex. Further information on the vortex lattice method used here can be found by Katz and Plotkin (2001). Propeller, fuselage, and stabilizers are not included in the analysis, and the resulting aerodynamic mesh is given in the center of Fig. 2.

Drag computations present a problem for this inviscid modeling technique, which can only provide induced drag due to lift (the downwash of the finite span deflects the local velocity vector at each wing section downward, tilting the lift vector slightly backward to provide a small drag force): drag due to flow separation and viscous shear is unaccounted for. The latter terms are included by augmenting the drag with a nonzero C_{Do}, estimated from experimental data to be 0.05. The viscous drag terms are not truly constant (flow separation generally increases with angle of attack, for example), and so the vortex lattice method is expected to under-predict the overall drag. Previous work has shown this method to provide an adequate computation of drag (as well as lift and pitching moments) at moderate angles of attack, as compared to wind tunnel data, for micro air vehicle wings (Stanford et al. 2007a). It should also be noted here that higher-fidelity aerodynamic modeling techniques are available: unsteady methods that model the wing-wake interactions, as well as panel methods suitable for simulations of entire vehicles.

Aeroelastic coupling is facilitated by considering the system as defined by a three field response vector $\mathbf{r}$:

$$\mathbf{r} = \left\{ \mathbf{u}^T \ \mathbf{z}^T \ \mathbf{\Gamma}^T \right\}^T \tag{7}$$

where $\mathbf{u}$ is the solution to the system of finite element equations (composed of both displacements and rotations) at each free node, $\mathbf{z}$ is the shape of the flexible wing, and Γ is the vector of unknown horseshoe vortex circulations (the solution vector of (5)). The coupled system of equations $\mathbf{G}(\mathbf{r})$ is then:

$$\mathbf{G}(\mathbf{r}) = \begin{Bmatrix} \mathbf{K} \cdot \mathbf{u} - \mathbf{Q} \cdot \mathbf{\Gamma} \\ \mathbf{z} - \mathbf{z}_o - \mathbf{P} \cdot \mathbf{u} \\ \mathbf{C} \cdot \mathbf{\Gamma} - \mathbf{L} \end{Bmatrix} = \mathbf{0} \tag{8}$$

The first row of $\mathbf{G}$ is the finite element analysis: $\mathbf{K}$ is the stiffness matrix assembled from the elemental matrices, and appropriately reduced based upon fixed boundary conditions along the wing root. $\mathbf{Q}$ is an interpolation matrix that converts the circulation of each horseshoe vortex into a pressure, and subsequently into the transverse force at each free node. The second row of $\mathbf{G}$ is a simple grid regeneration analysis: $\mathbf{z}_o$ is the original (rigid) wing shape, and $\mathbf{P}$ is a second interpolation matrix that converts the finite element state vector into displacements at each free and fixed node along the wing. The third row of $\mathbf{G}$ is the vortex lattice method, rewritten from (5): $\mathbf{C}$ is the influence matrix depending solely on the wing geometry, and $\mathbf{L}$ is the source vector

depending on the wing's outward normal vectors, the angle of attack, and the free stream velocity. Convergence of this system can typically be obtained within 25 iterations, when the logarithmic error in the wing's lift coefficient is less than −5.

3.3 Adjoint sensitive analysis

As the number of variables in the aeroelastic system (essentially the density of each element) will always outnumber the constraints and objective functions, a sensitivity analysis can be most effectively carried out with an adjoint analysis. The sought-after total derivative of the objective function with respect to each density variable is given through the chain rule:

$$\frac{\mathrm{d}g}{\mathrm{d}\mathbf{X}} = \frac{\partial g}{\partial \mathbf{X}} + \frac{\partial g}{\partial \mathbf{r}}^T \cdot \frac{\mathrm{d}\mathbf{r}}{\mathrm{d}\mathbf{X}} \tag{9}$$

where g is the objective function and $\mathbf{r}$ is the aeroelastic state vector of (7). The term $\partial g/\partial \mathbf{X}$ is the explicit portion of the derivative, while the latter term is the implicit portion through dependence on the aeroelastic system (Haftka and Gürdal 1992). Only aerodynamic objective functions are considered in this work: the explicit portion is then zero, unless the intermediate density penalty (2) is included.

The derivative of the objective function with respect to the aeroelastic state vector is:

$$\frac{\partial g}{\partial \mathbf{r}} = \left\{ \mathbf{0} \quad \mathbf{0} \quad \mathbf{S}^T \right\}^T \tag{10}$$

where $\mathbf{S}$ is the derivative of the aerodynamic objective function with respect to the vector of horseshoe vortex circulations. For metrics such as lift and pitching moment, $g = \mathbf{S}^T \cdot \boldsymbol{\Gamma}$, though more complex expressions exist for drag-based metrics. The derivative of the aeroelastic state vector with respect to the element densities is found by differentiating the coupled system:

$$\frac{\mathrm{d}\mathbf{G}\left(\mathbf{X}, \mathbf{r}\right)}{\mathrm{d}\mathbf{X}} = \mathbf{0} \Rightarrow \frac{\partial \mathbf{G}}{\partial \mathbf{X}} + \mathbf{A} \cdot \frac{\mathrm{d}\mathbf{r}}{\mathrm{d}\mathbf{X}} = \mathbf{0} \tag{11}$$

Only the finite element analysis of the aeroelastic system contains the element densities, and so the derivative of the aeroelastic system with respect to the density variables is then:

$$\frac{\partial \mathbf{G}}{\partial \mathbf{X}} = \begin{bmatrix} \frac{\partial \mathbf{K}}{\partial \mathbf{X}} \cdot \mathbf{u} \\ \mathbf{0} \\ \mathbf{0} \end{bmatrix} \tag{12}$$

$\mathbf{A}$ is the Jacobian of the aeroelastic system, defined by:

$$\mathbf{A} = \frac{\partial \mathbf{G}}{\partial \mathbf{r}} = \begin{bmatrix} \mathbf{K} & \mathbf{0} & -\mathbf{Q} \\ -\mathbf{P} & \mathbf{I} & \mathbf{0} \\ \mathbf{0} & \mathrm{d}\mathbf{C}/\mathrm{d}\mathbf{z} \cdot \boldsymbol{\Gamma} - \partial \mathbf{L}/\partial \mathbf{z} & \mathbf{C} \end{bmatrix} \tag{13}$$

The terms from (10–13) are inserted into (9); the implicit portion of the derivative becomes a triple product which is solved with the adjoint method. The adjoint vector does not contain the density of each element ($\mathbf{X}$), and only needs to be solved once, as intended:

$$\mathbf{a} = \mathbf{A}^{-T} \cdot \frac{\partial g}{\partial \mathbf{r}} \tag{14}$$

Two three-dimensional tensors are required for the adjoint method. From a computational standpoint both are relatively sparse, but $\partial \mathbf{K}/\partial \mathbf{X}$ (12) is fairly inexpensive to compute (Haftka and Gürdal 1992), while $\mathrm{d}\mathbf{C}/\mathrm{d}\mathbf{z}$ (13) is very intensive, and represents a significant portion of the cost associated with the gradient calculations. The former term is mostly zero: as seen in Fig. 2, each quadrilateral wing panel is divided into two triangles. As such, $\partial \mathbf{K}/\partial \mathbf{X}_i$ only receives contributions from two element stiffness matrices, and the remainder of the assembled matrix is zero. The $\mathrm{d}\mathbf{C}/\mathrm{d}\mathbf{z}$ term is the derivative of the influence matrix with respect to the wing shape, and requires a sensitivity analysis of the Biot–Savart law. $\mathbf{z}$ is defined at the nodes of the mesh in Fig. 2, or the corners of each vortex panel. As such, a change in a single $\mathbf{z}_i$ will the change the geometrical position of up to four control points and four horseshoe vortices (both of which are defined within the panels): $\mathrm{d}\mathbf{C}/\mathrm{d}\mathbf{z}_i$ is then found to be a sparse matrix with up to four non-zero rows and columns.

The second derivative of the objective function is required if aerodynamic derivative metrics such as $C_{\mathrm{L}\alpha}$ and $C_{\mathrm{m}\alpha}$ are of interest. Two options are available for this computation. The first involves a similar analytical approach to the one described above. This would eventually necessitate the extremely difficult computation of $\partial \mathbf{A}/\partial \mathbf{r}$, which is seldom done in practice (Maute et al. 2002). For the current work, only $\mathbf{C}$ depends on the aeroelastic state vector, while the rest of the Jacobian would be zero. Nonetheless, this remaining term $\mathrm{d}^2\mathbf{C}/\mathrm{d}\mathbf{z}^2$ is a four-dimensional tensor, and the computational complexities and cost associated with its construction is expected to be severe. As an alternative, finite differences are used here:

$$\frac{\partial g^2}{\partial \mathbf{X} \partial \alpha} \approx \frac{1}{\Delta \alpha} \cdot \left(\frac{\partial g}{\partial \mathbf{X}} (\alpha + \Delta \alpha) - \frac{\partial g}{\partial \mathbf{X}} (\alpha) \right) \tag{15}$$

The term $\partial g/\partial \alpha$ can be computed using another finite difference, or with the adjoint method described above, substituting the angle of attack for the element densities $\mathbf{X}$.

In order to solve the linear system of the Jacobian matrix, a staggered approach is adapted, rather than solving the entire system of (un-symmetric sparse) equations as a whole (Maute et al. 2002). Each

sub-problem is solved with the same algorithm used in the aeroelastic solver (direct sparse solver for the finite element equations, and an iterative Gauss–Seidel solver for the vortex lattice equations), and as such, the computational cost and number of iterations needed for convergence is approximately equal between the aeroelastic solver and the adjoint vector solver. The size of the numerical system is moderate: each optimization iteration requires ~3 min of simulation time on a Compaq Alpha workstation with a UNIX OSF1 V5.0 910 operating system (for the 30 × 30 grid over the semi-wing, as seen in Fig. 2), with construction of $d\mathbf{C}/d\mathbf{z}$ allocated about 50% of this time. The computational cost can be expected to decrease for stiffer wings.

3.4 Optimization framework

In order to ensure the existence of the optimal wing topologies, a mesh-independent filter is employed. Such a filter acts as a moving average of the gradients throughout the membrane wing, and limits the minimum size of the imbedded carbon fiber structures (Bendsøe and Sigmund 2003). As no constraints are included in the optimization, an unconstrained Fletcher–Reeves conjugate gradient algorithm (Haftka and Gürdal 1992) is employed. Step size is kept constant, at a reasonably small value to preserve the fidelity of the sensitivity analysis. In order to increase the chances of locating a global optimum, each optimization is run with three distinct initial designs: $\mathbf{X}_o = 1$ (carbon fiber wing), $\mathbf{X}_o = 0.5$, and $\mathbf{X}_o = 0.1$. A pure membrane wing ($\mathbf{X}_o = 0$) cannot be considered for reasons discussed above.

4 Results

Five objective functions are considered in this work: two load-augmenting metrics (maximum lift and minimum $C_{m\alpha}$), two load-alleviating metrics (minimum drag, and minimum $C_{L\alpha}$) and efficiency (maximum L/D). The MAV wing under consideration has a Zimmerman planform, with a 152 mm wingspan, 124 mm root chord, and an aspect ratio of 1.25.7° of positive geometric twist (nose up) is built into the wingtip, with 7° of dihedral between $2y/b = 0.4$ and the wingtip. Both a reflex airfoil and a singly-curved airfoil are studied (the former mitigates the pitching moment of the wing, and allows for the removal of a horizontal stabilizer to decrease the size of the MAV). Both have a maximum camber at the root of 6.8% (at $x/c = 0.22$), and the former airfoil has a maximum reflex at the root of −1.4% (at $x/c = 0.86$). Flight speed is kept constant at 13 m/s (equating to a Reynolds number of 10^5), but both 3° and 12° angles of attack are considered, with a $\Delta\alpha$ of 1° for finite differences. The flexural rigidity of the carbon fiber laminates is 0.5 N·m, and the pre-stress resultant of the latex membrane is 7 N/m. The thickness of the former is 0.5 mm, and the latter is 0.1 mm.

A typical convergence history of the aeroelastic topology optimizer can be seen in Fig. 4, for a reflex wing at 3° angle of attack, with a maximum L/D objective function. Results are computed with a 30 ×

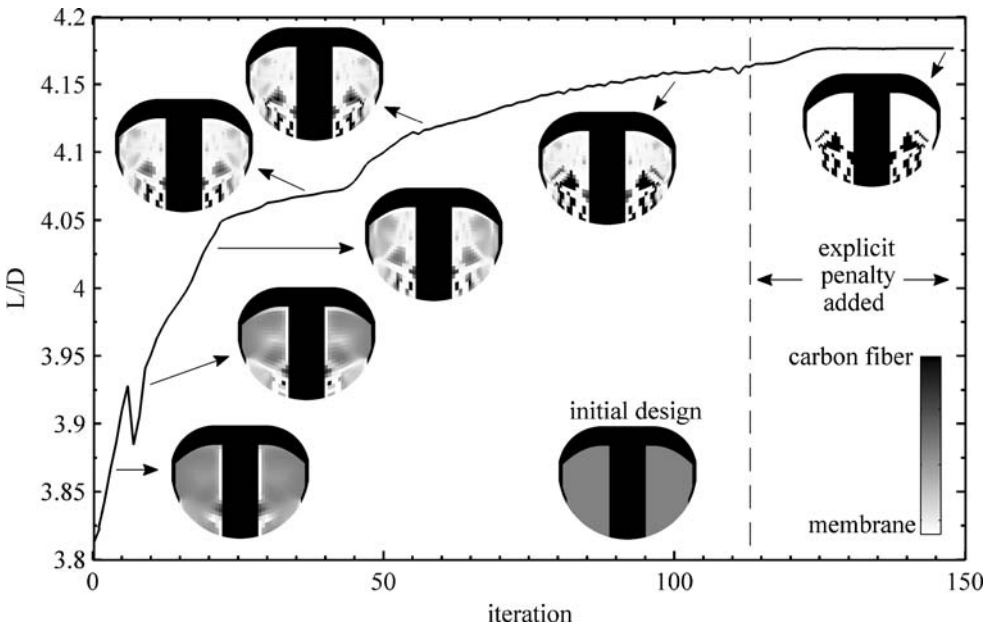

Fig. 4 Convergence history for maximizing L/D, $\alpha = 3°$, reflex wing (30 × 30 grid over the semi-wing)

30 grid over the semi-wing, and the initial guess is an intermediate density of 0.5. Within four iterations, the optimizer has removed all of the carbon fiber adjacent to the root of the wing, with the exception of the region located at three-quarters of the chord, which corresponds to the inflection point of the reflex airfoil. The material towards the leading edge and at the wing tip is also removed. Further iterations see topological changes characterized by intersecting threads of membrane material that grow across the surface, leaving behind "islands" of carbon fiber. These structures aren't connected to the laminate wing, but are imbedded within the membrane skin.

These results indicate two fundamental differences between the designs in Fig. 1 and those computed via aeroelastic topology optimization. The first is the presence of "islands"; these designs can be built, but the process is significantly more complicated than with a monolithic wing skeleton. Such structures could be avoided with a manufacturability constraint/objective function (such as discussed by Lyu and Saitou (2005)), but the logistics of such a metric are difficult to formulate. Furthermore, the aeroelastic advantages of free-floating laminate structures are significant, as will be discussed below. A second difference is the fact that the designs of Fig. 1 are composed entirely from thin strips of carbon fiber embedded within the membrane, while the topology optimization is apt to utilize two-dimensional laminate structures.

After 112 iterations in Fig. 4, the optimization has largely converged (with only minimal further improvements in L/D), but some material with intermediate densities remains towards the leading edge of the wing. Many techniques exist for effectively interpreting gray level topologies (Hsu and Hsu 2005); the explicit penalty of (2) is used here. Surprisingly, the L/D sees a further increase with the addition of this penalty, contrary to the conflict between performance and 0–1 convergence reported by Chen and Wu (2008). The explicit penalty does not significantly alter the topology, but merely forces all of the design variables to their limits, as intended.

The final wing skeleton has three trailing edge battens (one of which is connected to a triangular structure towards the center of the membrane skin), and a fourth batten oriented at 45° to the flow direction. The structure appears to be a topological combination of a BR and a PR wing, with both battens and membrane inflation towards the leading edge. The optimized topology increases the L/D by 9.5% over the initial design, and (perhaps more relevant, as the initial intermediate-density design does not technically exist) by 10.2% over the rigid wing.

The affect of mesh density is given in Fig. 5, for a reflex wing at 12° angle of attack, with L/D maximization as the objective function. The 30 × 30 grid, for example, indicates that 900 vortex panels (and 1,800 finite elements) cover each semi-wing. As the leading edge, root, and wing tip of each wing are fixed as carbon fiber, 480 density design variables are left for the topology optimization. One obvious sign of adequate convergence is the efficiency of the rigid wing, with only a 0.44% difference between that computed on the two finer grids. The optimal wing topologies in Fig. 5 are similar, with three distinct carbon fiber structures imbedded within the membrane skin. While the 20 × 20 grid is certainly too coarse to adequately resolve the geometries of interest, the topology computed on the 30 × 30 grid is very similar to that computed on the 40 × 40 grid. The computational cost of each optimization iteration upon the coarser grid is five times less than that seen for a 40 × 40 grid, and will be used for the remainder of this work.

The affect of the initial starting design is given in Fig. 6, for a reflex wing at 12° angle of attack, with drag minimization as the objective function. As mentioned above, $\mathbf{X}_o = 1$ (carbon fiber wing), $\mathbf{X}_o = 0.5$, and $\mathbf{X}_o = 0.1$ are all considered. The three final optimal topologies are very different, indicating a large dependency upon the initial guess and no guarantee that a global

Fig. 5 Affect of mesh density upon optimal L/D topology, $\alpha = 12°$, reflex wing

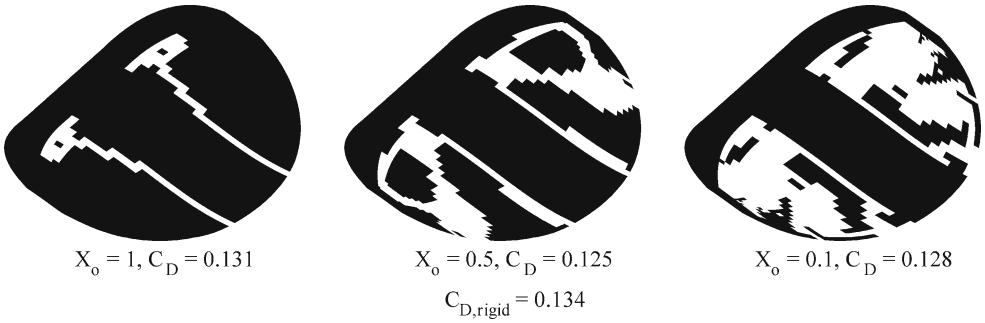

Fig. 6 Affect of initial design upon the optimal C_D topology, $\alpha = 12°$, reflex wing

optimum has been located. Nevertheless, the indicated improvements in drag are promising, with a potential 6.7% decrease from the rigid wing. As expected, the denser the initial topology, the denser the final optimized topology.

All three wing topologies utilize some form of adaptive washout for load and drag alleviation. The structures must be flexible enough to generate sufficient nose-down rotation of each wing section, but not so flexible that the membrane areas of the wing will inflate and camber, increasing the forces. The wing structure in the center of Fig. 6 (with $\mathbf{X}_o = 0.5$) strikes the best compromise between the two deformations, and provides the lowest drag. When $\mathbf{X}_o = 1$, the structure is too stiff, relying upon a membrane hinge between the carbon fiber wing and root. When $\mathbf{X}_o = 0.1$, the optimizer is unable to fill in enough space with laminates to prevent membrane inflation. Of the three designs, this is the least tractable from a manufacturing point of view as well.

The dependency of the optimal topology (maximum lift) upon both angle of attack and airfoil shape are given in Fig. 7, for both a reflex (left two plots) and a cambered wing (right two plots). For the wing with trailing edge reflex, the optimal lift design looks similar to that found in Fig. 4: trailing edge battens that extend no farther up the wing than the half-chord, a spanwise member that coincides with the inflection point of the airfoil, and unconstrained membrane skin towards the leading edge, where the forces are largest. The optimizer has realized that it can maximize lift by both cambering the wing through inflation at the leading edge, and forcing the trailing edge battens downward for wash-in.

This latter deformation is only possible due to the reflex (negative camber) in this area, included to offset the nose-down pitching moment of the remainder of the "flying wing", and thus allow for removal of a horizontal stabilizer due to size restrictions. Increasing the angle of attack from 3° to 12° shows no significant difference in the wing topology, slightly increasing the length of the largest batten. At the lower angle of attack, up to 22% increase in lift is indicated through topology optimization.

For the cambered wing (singly-curved airfoil, right two plots of Fig. 7), the lift over the rigid wing is, as expected, much larger than found in the reflex wings, but adequate stability becomes critical. With the removal of the negatively-cambered portion of the airfoil, most of the forces generated over this wing will be positive, and the topology optimizer can no longer gain additional lift via wash-in. Imbedding batten structures in the trailing edge will now result in washout, surely decreasing the lift. As such, the optimizer produces a trailing edge member that outlines the planform and connects to the root (similar to the perimeter-reinforced wing designs), restraining the motion of the trailing edge and inducing an aerodynamic twist.

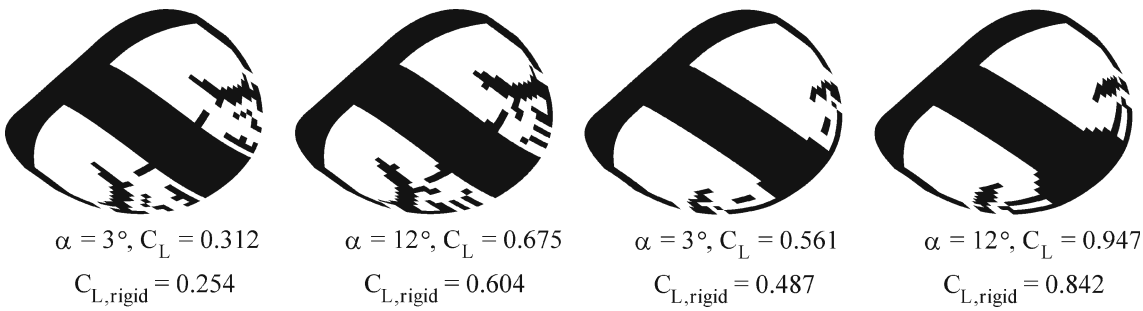

Fig. 7 Affect of angle of attack and airfoil upon the optimal C_L topology

Unlike the PR wing, this trailing edge reinforcement does not extend continuously from the root to the tip, instead ending at 65% of the semi-span. This is then followed by a trailing edge batten that extends into the membrane skin, similar to the designs seen for the reflex wing in Fig. 7. Why such a configuration should be preferred over the PR wing design for lift enhancement will be discussed below. As before, increasing the angle of attack has little bearing on the optimal topology, again increasing the size of the trailing edge batten. A potential increase in lift by 15% over the rigid wing is indicated at the lower angle of attack.

Similar results are given in Fig. 8, with L/D maximization as the topology design metric. Presumably due to the conflictive nature of the ratio, the wing topology that maximizes L/D is a strong function of angle of attack. For the reflex wing at lower angles, the optimal design resembles topologies used above for lift enhancement (Fig. 7), while at 12° the design is closer in topology to one with minimum drag (Fig. 6). Increasing lift is more important to L/D at lower angles, while decreasing drag becomes key at larger angles. The drag is very small at low angles of attack (technically zero for this inviscid formulation, if not for the inclusion of a constant $C_{Do)}$, and insensitive to changes via aeroelasticity.

This concept is less true for the cambered wing (right two plots of Fig. 8), where designs at both 3° and 12° angle of attack utilize a structure with trailing edge adaptive washout. At the lower angle, the topology optimizer leaves a large triangular structure at the trailing edge (connected to neither the root nor the wing tip), and the leading edge is filled in with carbon fiber. At the higher angle of attack, four batten-like structures are placed within the membrane skin, oriented parallel to the flow, one of which connects to the wing tip. Potential improvements are generally smaller than those seen above, though a 10% increase in L/D is available for the cambered wing at 12°.

Wing displacements and pressure distributions are given for select wing designs in Fig. 9, for a reflex wing at 12° angle of attack. Corresponding data along the spanwise section $2y/b = 0.58$ is given in Fig. 10. As the wing is modeled with no thickness in the vortex lattice method, distinct upper and lower pressure distributions are not available, only differential terms. Five topologies are discussed, beginning with a pure carbon fiber wing. Lift-augmentation designs are represented by a baseline PR wing and the topology optimized for maximum lift. Lift-alleviation designs are represented by a baseline BR wing and the topology optimized for minimum lift slope.

The differential pressure distribution over the monolithic carbon fiber wing is defined by leading edge suction due to flow stagnation, pressure recovery (and peak lift) over the maximum camber, and negative forces over the reflex portion of the wing. As expected, the inviscid solver misses the low-pressure cells at the wingtip (from the vortex swirling system), and the plateau in the pressure distribution, indicative of a separation bubble. This aerodynamic loading causes a moderate wash-in of the carbon fiber wing (0.1°), resulting in a computed lift coefficient of 0.604.

Computed deformation of the PR wing is much larger than the carbon fiber wing, though the deformations are within the range of validity of a linear finite element solver. The sudden changes in wing geometry at the membrane/carbon fiber interfaces lead to sharp downward forces at the leading and trailing edges, the latter of which exacerbates the effect of the airfoil reflex. Despite this, the membrane inflation increases the camber of the wing and thus the lift, by 6.5% over the carbon fiber wing.

Several disparate deformation mechanisms contribute to the high lift of the MAV design located by the aeroelastic topology optimizer (middle column, Fig. 9). First, the membrane inflation towards the leading edge increases lift via cambering, similar to the PR wing (the

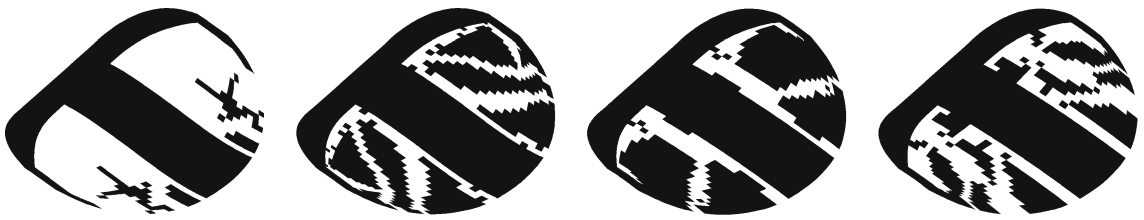

Fig. 8 Affect of angle of attack and airfoil upon the optimal L/D topology

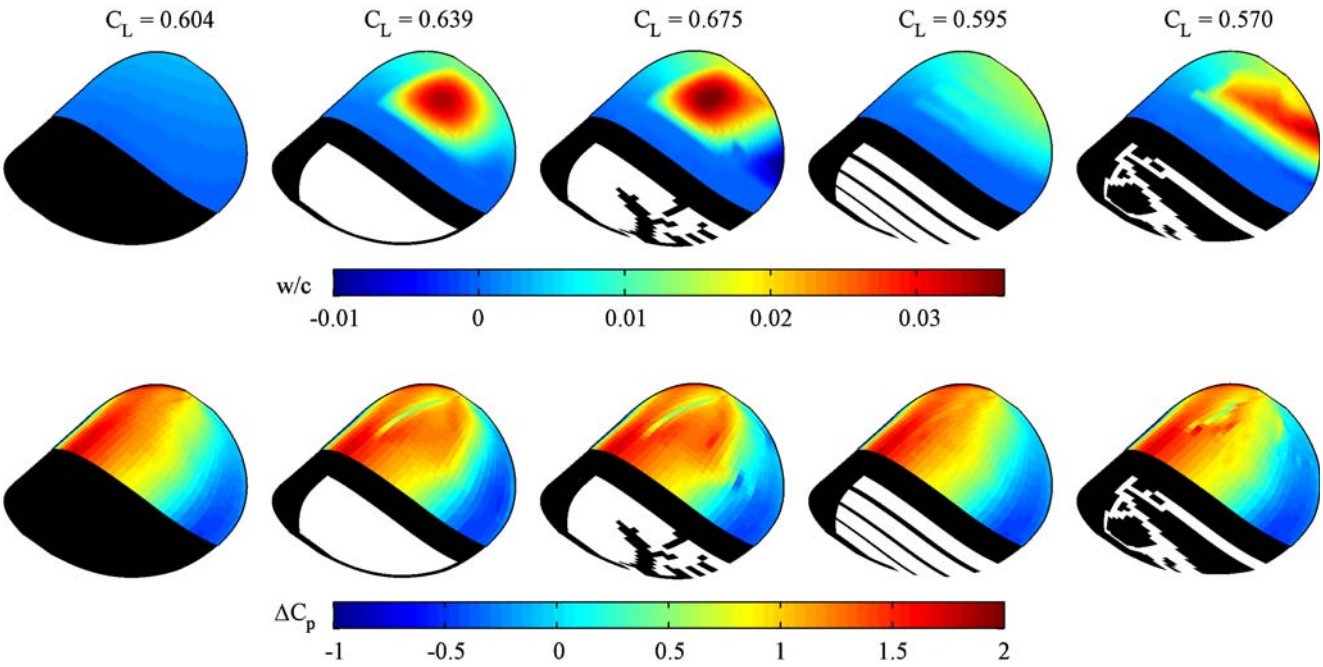

Fig. 9 Normalized out-of-plane displacements (*top*) and differential pressure coefficients (*bottom*) for baseline and optimal topology designs, $\alpha = 12°$, reflex wing

pressure distributions over the two wing structures are identical through $x/c = 0.25$). The main trailing edge batten structure is then depressed downward along the trailing edge (due to the reflex) for wash-in, increasing the local angle of attack of each flexible wing section, and thus the lift. It can also be seen (from the left side of Fig. 10 in particular) that the local bending/twisting of this batten structure is minimal: the deformation along this structure is largely linear down the wing. The intersection of this linear trend with the curved inflated membrane shape produces a cusp in the airfoil. The small radius of curvature forces very large velocities, resulting in the lift spike at 46% of the chord.

This combination of wash-in and cambering leads to a design which out-performs the lift of the PR wing by 5.6%, but the former effect is troubling. The wash-in essentially removes the reflex from the airfoil (as does the aerodynamic twist of the PR wing), an attribute originally added to mitigate the nose-down pitching moment. This fact leads to two important ideas. First, thorough optimization of a single design metric is ill-advised for micro air vehicle design, as other aspects of

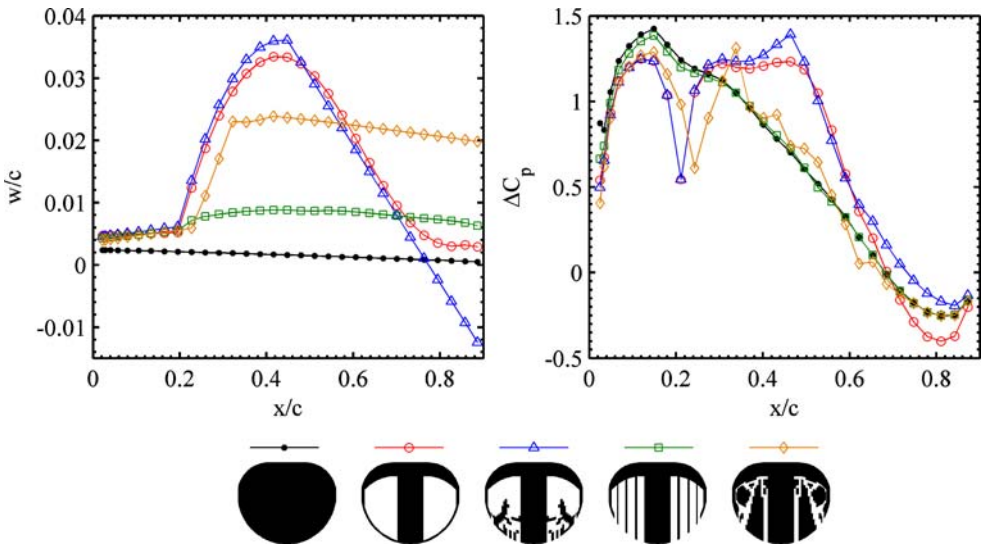

Fig. 10 Deformations and pressures along $2y/b = 0.58$ for baseline and optimal topology designs, $\alpha = 12°$, reflex wing

the flight performance will surely degrade. Its inclusion here is only meant to emphasize the relationship between aeroelastic deformation and flight performance, and show the capabilities of the topology optimization. Secondly, if the design goal is a single-minded maximization of lift, a reflex airfoil is a poor choice compared to a singly-curved airfoil, a shape which the topology optimizer strives to emulate through aeroelastic deformations.

Referring now to the load-alleviating MAV wing structures of Figs. 9 and 10, the deformation of the BR wing is relatively small, allowing for just 0.1° of adaptive washout. The BR wing is very sensitive to pre-tensions in the span direction; the structure is too stiff. Furthermore, the reflex in the wing pushes the trailing edge down, limiting the ability of the battens to washout for load reduction. Less than a 2% drop in lift from the carbon fiber wing is obtained, and the pressure distributions of the two wings in Fig. 10 are very similar.

The load alleviating design located by the topology optimizer (right column, Fig. 9) is significantly more successful. By filling the design space with patches of disconnected carbon fiber structures (dominated by a long batten which extends the length of the membrane skin, but is not connected to the wing's leading edge), the MAV wing is very flexible, but none of the membrane portions of the wing are large enough to camber the wing via inflation. Wing deformation is the same magnitude as that seen in the PR-type wings, but the motion is located at the trailing edge for adaptive washout, and lift is decreased by 5%. The local deformation within the membrane between the leading edge and the long batten structure is substantial, and the flow deceleration over this point sees a further loss in lift, as with the PR wing.

Similar results are given in Figs. 11 and 12, for a cambered wing at 12° angle of attack. The three baseline wings are again shown (carbon fiber wing, PR, and BR), as well as the designs located by the topology optimization to maximize lift and minimize lift slope. As the forces are generally larger for the cambered airfoil, the deformations have increased to 5% of the root chord. The negative forces at the trailing edge of the airfoil are likewise absent. As before, the PR membrane wing effectively increases the lift over its carbon fiber counterpart through adaptive cambering, along with aerodynamic penalties from the shape discontinuities at the leading and trailing edge of the membrane skin.

There is an appreciable amount of upward deformation of the PR wing's trailing edge carbon fiber strip, leading to washout of each flexible wing section, degrading the lift. As such, the aeroelastic topology optimizer can maximize lift (Fig. 11, middle column) by adding more material to this strip and negating the motion of the trailing edge. As discussed above, this strip

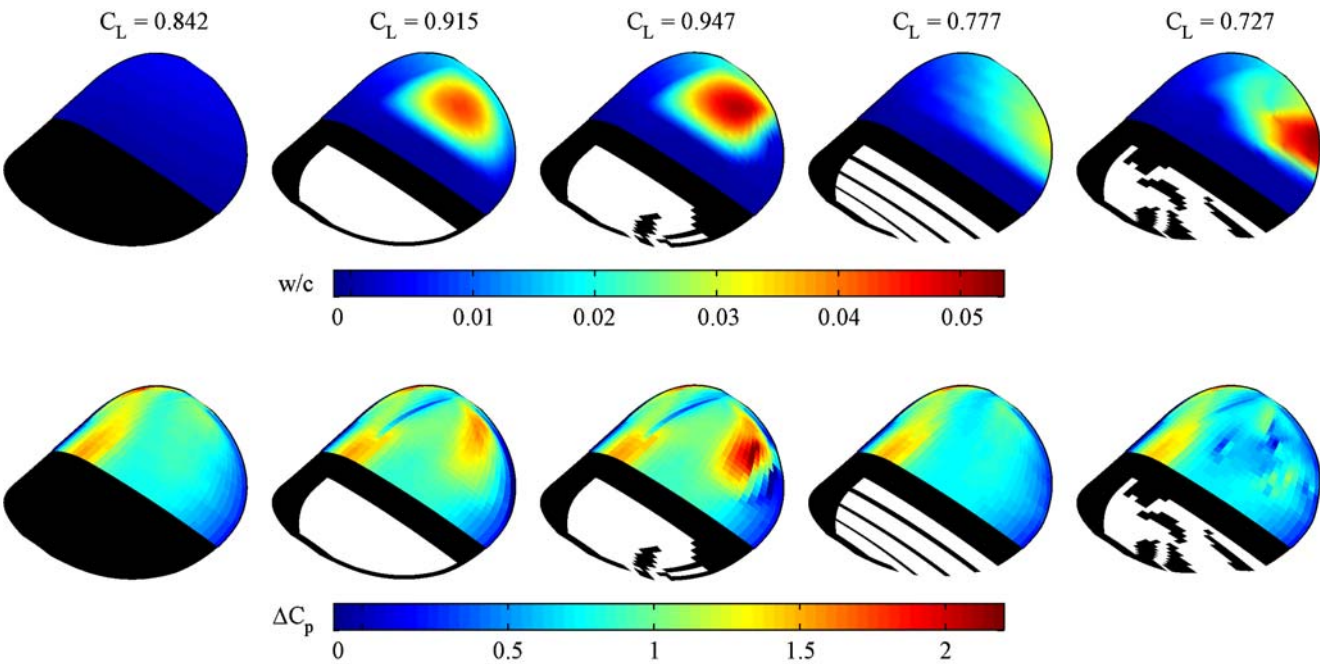

Fig. 11 Normalized out-of-plane displacements (*top*) and differential pressure coefficients (*bottom*) for baseline and optimal topology designs, $\alpha = 12°$, cambered wing

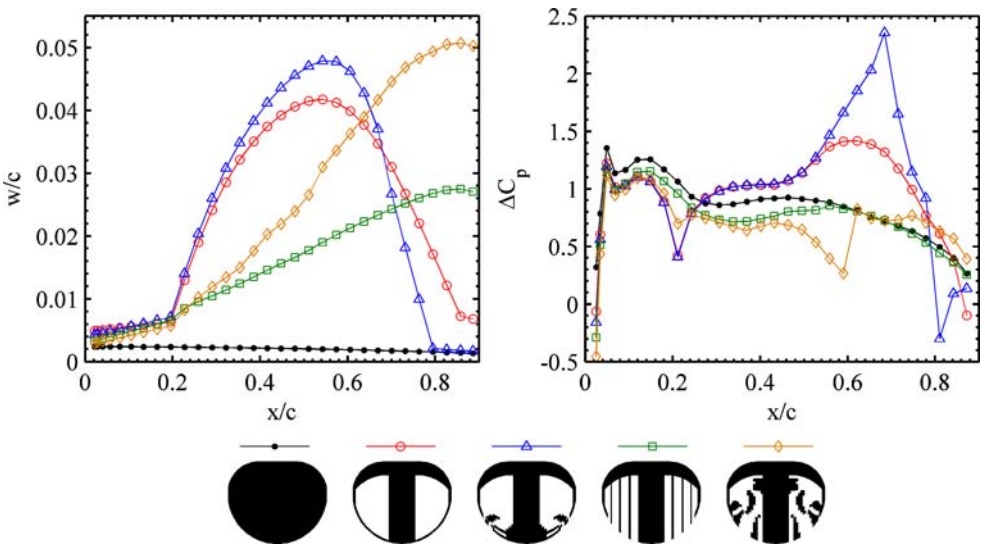

Fig. 12 Deformations and pressures along $2y/b = 0.58$ for baseline and optimal topology designs, $\alpha = 12°$, cambered wing

does not continue unbroken to the wing tip, but ends at 65% of the semispan. The remaining membrane trailing edge is filled with a free-floating carbon fiber batten. Such a configuration can (theoretically) improve the lift in several ways, similar to the trailing edge structure used for lift optimization in Fig. 9.

Placing a flexible membrane skin between two rigid supports produces a trade-off: the cambering via inflation increases lift, but this metric is degraded by the sharp discontinuities in the airfoil shape. Towards the inner portion of the MAV wing, this trade-off is favorable for lift. Towards the wingtip however (either due to the changes in chord or in pressure) this is no longer true: the total lift can be increased by allowing this portion of the trailing edge to washout, thereby avoiding the negative pressures seen elsewhere along the trailing edge.

The forward portion of this batten structure also produces a cusp in the wing geometry, forcing a very strong low pressure spike over the upper portion of the airfoil to increase the lift, as before. The inviscid solver probably over-predicts the strength of this spike: the presence of viscosity will attenuate the speed of the flow, and thus both the magnitude of the low pressure spike and its beneficial effect upon lift. The aeroelastic topology optimizer predicts a 3.5% increase in lift over the PR wing, and 12.5% increase over the carbon fiber wing, though the veracity of these comparisons requires a viscous solver to ascertain the actual height of the low-pressure spike at $x/c = 0.68$.

The batten-reinforced design of Fig. 11 is substantially more effective with the cambered wing, largely due to the positive forces at the trailing edge (rather than the negative forces seen over the reflex wing). The

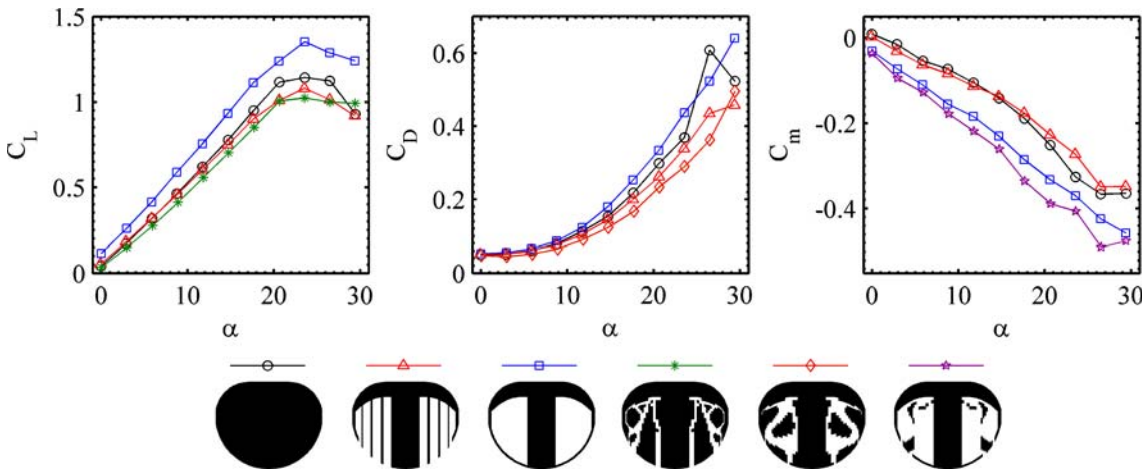

Fig. 13 Experimentally measured forces and moments for baseline and optimal topology designs, reflex wing

1.6° of washout in the cambered BR wing decreases the load throughout most of the wing and decreases the lift by 8.5% (compared to the carbon fiber wing), but, as before, the load-alleviating design located by the topology optimizer (right column, Fig. 11) is superior. Similar to above, the design utilizes a series of disconnected carbon fiber structures, oriented parallel to the flow, and extending to the trailing edge. The discontinuous wing surface forces a number of high-pressure spikes on the upper surface, notably at x/c = 0.2 and 0.6. This, in combination with the substantial adaptive washout at the trailing edge, decreases the lift by 13.6% over the carbon fiber wing and by 5.6% over the BR wing.

5 Experimental validation

Due to the low-fidelity nature of the aeroelastic analysis employed in this work, a certain measure of experimental validation of the superiority of computed optima over baseline designs is required. This is particularly true for drag-based metrics, which, as discussed above, the vortex lattice method with struggle to accurately compute. For this purpose, six designs are built for experimental testing: three baseline designs (monolithic carbon fiber wing, PR, and BR wings), and three topologically-optimized designs (minimum $C_{L\alpha}$, minimum drag, and minimum $C_{m\alpha}$, the third, fourth, and fifth wings shown in Fig. 13). The latter three designs are found by optimizing with a reflex airfoil, at 3° angle of attack. All testing is conducted in a closed-loop wind tunnel, and loads are measured with a strain gage sting balance through an entire α-sweep; more details pertaining to the experimental testing can be found by Stanford et al. (2007a).

Experimental results are given in Fig. 13, in terms of C_L, C_D, and C_m of the three baseline designs and the relevant optimal design. All three structures located by the topology optimizer show marked improvements over the baseline experimental data, validating the use of a low fidelity aeroelastic model as a surrogate for computationally-intensive nonlinear models. With the exception of very low (where deformations are small) and very high angles of attack (where the wing has stalled), the optimized designs consistently out-perform the baselines. The minimum $C_{L\alpha}$ design has a shallower lift slope than the BR wing, and a flatter stalling curve (left of Fig. 13). The minimum drag design similarly out-performs the BR wing (middle of Fig. 13). The minimum $C_{m\alpha}$ design has a steeper pitching moment slope than the PR wing (right of Fig. 13), indicative of a longer static stability margin.

6 Conclusions

Aeroelastic topology optimization has been used to design the laminate reinforcement of a membrane micro air vehicle wing, with a two-material formulation of the wetted surface. The static aeroelasticity is modeled with a vortex lattice method coupled to linear membrane and shell elements. The sensitivity of the wing's aerodynamic performance to each element density is computed with an adjoint analytical sensitivity analysis. The following conclusions can be drawn:

1. Nonlinear power-law interpolation between 0 (membrane) and 1 (carbon fiber) ensures a smooth aeroelastic response.
2. An explicit penalty based upon the sine function adequately pushes the design to a 0–1 distribution without significantly altering topology.
3. The optimal solution is very dependent upon the initial topology, requiring multiple runs for each case.
4. Optimal lift- and drag-based metrics are insensitive to flight condition, though L/D is not.
5. The optimizer makes use of several disparate phenomena for lift augmentation: membrane inflation to camber the wing, depression of the trailing edge for wash-in, and sharp cusps in surface geometry that cause the pressure to locally spike.
6. Optimal load-alleviation is obtained with a series of disjointed laminate structures: the wing is flexible enough to substantially washout at the trailing edge, but the remaining membrane patches aren't large enough to locally inflate, which would add camber and increase the lift.
7. Relevant improvements in aerodynamic performance can be obtained despite the low-fidelity aeroelastic model employed, as indicated by experimental testing.

This work has clearly demonstrated the feasibility of aeroelastic topology optimization for membrane wings, but future work would need to concentrate on several areas. First, multi-objective analysis is required to locate designs with adequate performance along a wide range of flight conditions. Secondly, it is hypothesized here that minimizing the lift slope will help with gust alleviation as well, but the veracity of this claim needs to be tested with unsteady aeroelastic models and non-homogenous incoming flow. Finally, agility-based metrics should be considered as well: a MAV wing in a lateral roll maneuver, for example.

Acknowledgements This work was jointly supported by the Air Force Research Laboratory and the Air Force Office of Scientific Research under the MURI program F49620-03-1-0381.

References

Albertani R, Stanford B, Hubner J, Ifju P (2007) Aerodynamic coefficients and deformation measurements on flexible micro air vehicle wings. Exp Mech 47(5):625–635

Anagnostou G, Rønquist E, Patera A (1992) A computational procedure for part design. Comput Methods Appl Mech Eng 97(1):33–48

Balabanov V, Haftka R (1996) Topology optimization of transport wing internal structure. J Aircr 33(1):232–233

Beckers M (1999) Topology optimization using a dual method with discrete variables. Struct Multidisc Optim 17(1):14–24

Bendsøe M, Sigmund O (2003) Topology optimization. Springer, Berlin, Germany

Bendsøe M, Lund E, Olhoff N, Sigmund O (2005) Topology optimization: broadening the areas of application. Control Cybern 34(1):7–35

Borrvall T, Petersson J (2003) Topology optimization of fluids in stokes flow. Int J Numer Methods Fluids 41(1):77–107

Chen T, Wu S (2008) Multiobjective optimal topology design of structures. Comput Mech 21(6):483–492

Cook R, Malkus D, Plesha M, Witt R (2002) Concepts and applications of finite element analysis. Wiley, New York, NY

Deb K, Goel T (2001) A hybrid multi-objective evolutionary approach to engineering shape design. In: International conference on evolutionary multi-criterion optimization, 7–9 March, Zurich, Switzerland

Eschenauer H, Olhoff N (2001) Topology optimization of continuum structures: a review. Appl Mech Rev 54(4):331–390

Gersborg-Hansen A, Sigmund O, Haber R (2005) Topology optimization of channel flow problems. Struct Multidisc Optim 30(3):181–192

Gomes A, Suleman A (2008) Topology optimization of a reinforced wing box for enhanced roll maneuvers. AIAA J 46(3):548–556

Haftka R, Gürdal Z (1992) Elements of structural optimization. Kluwer, Dordrecht, The Netherlands

Hsu M, Hsu Y (2005) Interpreting three-dimensional structural topology optimization results. Comput Struct 83(4):327–337

Katz J, Plotkin A (2001) Low-speed aerodynamics. Cambridge University Press, Cambridge, UK

Krog L, Tucker A, Kemp M (2004) Topology optimization of aircraft wing box ribs. In: AIAA/ISSMO multidisciplinary analysis and optimization conference, 30 August–1 September, Albany, NY

Lee S, Bae J, Hinton E (2000) Shell topology optimization using the layered artificial material model. Int J Numer Methods Eng 47(4):843–867

Luo Z, Yang J, Chen L (2006) A new procedure for aerodynamic missile designs using topological optimization approach of continuum structures. Aerosp Sci Technol 10(5):364–373

Lyu N, Saitou K (2005) Topology optimization of multicomponent beam structure via decomposition-based assembly synthesis. J Mech Des 127(2):170–183

Martins J, Alonso J, Reuther J (2001) Aero-structural wing design optimization using high-fidelity sensitivity analysis. In: Confederation of European aerospace societies conference on multidisciplinary analysis and optimization, 25–26 June, Cologne, Germany

Maute K, Allen M (2004) Conceptual design of aeroelastic structures by topology optimization. Struct Multidisc Optim 27(1):27–42

Maute K, Reich G (2006) Integrated multidisciplinary topology optimization approach to adaptive wing design. J Aircr 43(1):253–263

Maute K, Nikbay M, Farhat C (2002) Sensitivity analysis and design optimization of three-dimensional non-linear aeroelastic systems by the adjoint method. Int J Numer Methods Eng 56(6):911–933

Ormiston R (1971) Theoretical and experimental aerodynamics of the sail wing. J Aircr 8(2):77–84

Pingen G, Evgrafov A, Maute K (2007) Topology optimization of flow domains using the Lattice Boltzmann method. Struct Multidisc Optim 34(6):507–524

Stanford B, Abdulrahim M, Lind R, Ifju P (2007a) Investigation of membrane actuation for roll control of a micro air vehicle. J Aircr 44(3):741–749

Stanford B, Sytsma M, Albertani R, Viieru D, Shyy W, Ifju P (2007b) Static aeroelastic model validation of membrane micro air vehicle wings. AIAA J 45(12):2828–2837

Stegmann J, Lund E (2005a) Nonlinear topology optimization of layered shell structures. Struct Multidisc Optim 29(5):349–360

Stegmann J, Lund E (2005b) Discrete material optimization of general composite shell structures. Int J Numer Methods Eng 62(14):2009–2027

Stolpe M, Stidsen T (2006) A hierarchical method for discrete structural topology design problems with local stress and displacement constraints. Int J Numer Methods Eng 69(5):1060–1084

Torres G (2002) Aerodynamics of low aspect ratio wings at low Reynolds numbers with applications to micro air vehicle design. Ph.D. Dissertation, Department of Aerospace and Mechanical Engineering, University of Notre Dame, South Bend, IN

Wang S, Tai K, Wang M (2006) An enhanced genetic algorithm for structural topology optimization. Int J Numer Methods Eng 65(1):18–44

Zuo K, Chen L, Zhang Y, Yang J (2007) Study of key algorithms in topology optimization. Int J Adv Manuf Technol 32(7):787–796